Journal of Computational Physics 228 (2009) 4625–4637

Contents lists available at ScienceDirect

Journal of Computational Physics

journal homepage: www.elsevier.com/locate/jcp

A high-order boundary integral method for surface diffusions on elastically stressed axisymmetric rods

Xiaofan Li [a,*], Qing Nie [b]

[a] Department of Applied Mathematics, Illinois Institute of Technology, 10 West 32nd Street, Chicago, IL 60616, USA
[b] Center for Mathematical and Computational Biology, Department of Mathematics, University of California, Irvine, CA 92697-3875, USA

ARTICLE INFO

Article history:
Received 8 November 2008
Received in revised form 16 March 2009
Accepted 21 March 2009
Available online 29 March 2009

MSC:
65R20
65M99
65B10
65B15
74B99

Keywords:
Boundary integral method
Axisymmetric domain
Integration factor methods
Surface diffusion
Elastic stress

ABSTRACT

Many applications in materials involve surface diffusion of elastically stressed solids. Study of singularity formation and long-time behavior of such solid surfaces requires accurate simulations in both space and time. Here we present a high-order boundary integral method for an elastically stressed solid with axi-symmetry due to surface diffusions. In this method, the boundary integrals for isotropic elasticity in axi-symmetric geometry are approximated through modified alternating quadratures along with an extrapolation technique, leading to an arbitrarily high-order quadrature; in addition, a high-order (temporal) integration factor method, based on explicit representation of the mean curvature, is used to reduce the stability constraint on time-step. To apply this method to a periodic (in axial direction) and axi-symmetric elastically stressed cylinder, we also present a fast and accurate summation method for the periodic Green's functions of isotropic elasticity. Using the high-order boundary integral method, we demonstrate that in absence of elasticity the cylinder surface pinches in finite time at the axis of the symmetry and the universal cone angle of the pinching is found to be consistent with the previous studies based on a self-similar assumption. In the presence of elastic stress, we show that a finite time, geometrical singularity occurs well before the cylindrical solid collapses onto the axis of symmetry, and the angle of the corner singularity on the cylinder surface is also estimated.

1. Introduction

Since the work by Nichols and Mullins [19], the deformation of a heated solid due to surface diffusion has been under many studies because of its broad applications. Driven by surface energy only (without elasticity), a thin solid cylinder is unstable to axi-symmetric perturbations when the wavelength exceeds the circumference of the unperturbed cylinder, and will pinch off forming a chain of spheres. The axi-symmetric pinchoff is self-similar and the cylinder forms conical shape at the pinchoff whose cone angle is universal, independent of the initial shape (for a review and the references, see Bernoff et al. [2]).

In the presence of stress in the solid, Asaro and Tiller [1] studied the surface evolution of a semi-finite elastic space subjected to a non-hydrostatic stress in two dimensions. Grinfeld [8] investigated the instability of the interface between a non-hydrostatic stressed elastic body and a melt. Spencer et al. [30] discussed the stability of a vapor-film interface and the effect of misfit strain. Chiu and Gao [4] considered the evolution of cycloid-type surfaces of a stressed elastic half-space. Spencer and Meiron [31] numerically simulated the nonlinear evolution of the stress-driven surface instability of a solid in two

* Corresponding author. Tel.: +1 312 567 5340.
E-mail addresses: lix@iit.edu (X. Li), qnie@math.uci.edu (Q. Nie).

0021-9991/$ - see front matter © 2009 Elsevier Inc. All rights reserved.
doi:10.1016/j.jcp.2009.03.024

dimensions. Panat et al. [22] studied the growth of surface perturbations induced by surface diffusion and bulk diffusion in a stressed solid.

For an axisymmetric solid, the linear stability analysis in Colin et al. [5] and Kirill et al. [14] and the numerical simulation of the fully nonlinear evolution of an axisymmetric cylinder in Li and Nie [17] demonstrated that the system develops short-wavelength instability when the applied stress is beyond a critical value. To study whether the instability leads to pinchoff or development of geometrical singularities in finite time, accurate calculations of the interface curvature, the elasticity energy and the temporal dynamics are needed.

The boundary integral method, which reduces the boundary value problems to a system of integral equations on the surface (or a curve), is particularly convenient and efficient for boundary value problems where Green's functions are known. In two dimensions, state-of-art spectrally accurate boundary integral methods have been developed for a wide variety of applications (for a review, see [11]). In axisymmetric domains, for systems with static boundaries, low-order methods have long been used for elasticity [13,18,6]; for moving interface problems, the integral calculation is usually of low order in Stokes flows (e.g., [23,32]) which have integral kernels similar to the isotropic elasticity; and, the integral calculations can be high-order (or adaptive) in potential flows because the singular kernels have relatively simple form [21,20]. The complex singularity forms of the axisymmetric Green's functions in the boundary integral equation of the elasticity or Stokes flows (for example, the two types of singularities, $1/r$ and $\ln r$, cannot be explicitly separated from the kernels) prevents direct applications of any existing high-order integral quadratures. For general smooth boundaries in three dimensions, a high-order boundary integral method for elliptic boundary value problems is presented in Ying et al. [34].

In this paper, to solve boundary integral equations for isotropic elasticity equations in axisymmetric settings, we apply a modified alternating point quadrature along with Richardson extrapolations to obtain a series of quadratures that can be of any odd orders. Furthermore, when the Green's functions are periodic in the axial direction, the evaluation of kernels usually dominates the overall simulation. To overcome this, we present a fast and accurate evaluation algorithm for the kernels using asymptotic expansions of the summations in terms of the number of summation periods and applying a recursive extrapolation technique.

In addition, the evolution equation involves a fourth-order derivative term due to the surface diffusion, yielding a severe numerical stability constraint on the size of time-steps when explicit temporal schemes are applied. On the other hand, any fully implicit schemes are computationally expensive as it is necessary to solve a large nonlinear system at each time step. In this paper, we present a high-order temporal scheme for interfaces in axisymmetric geometry based on the local decomposition technique and integration factor methods [10,25]. In this method, the fourth derivative term is integrated (in time) explicitly such that the constraint on the time-step is reduced significantly without increasing any computational cost.

With high-order accuracy in both space and time for the boundary integral method, we are able to study singularity formation for an elastically stressed periodic cylinder. Through direct numerical simulations, we find that in absence of elasticity the cylinder surface pinches at the axis of symmetry in a finite time, and the form of singularity is consistent with a previous study based on assumption of self-similarity of interface near pinchoff [2]. In presence of elasticity, our numerical simulations show that the cylinder surface develops a corner singularity in a finite time before it collapses onto the line of symmetry.

The paper is organized as follows: In Section 2, we present the governing equations of the system in which the stressed solid is periodic in axial direction and subject to uni-axial stress. In Section 3, we derive the boundary integral formulations of the system. In Section 4, we present detailed description of the numerical methods. In Section 5, we investigate the nonlinear evolution of the stressed cylinder and the singularity formation of the surface using the developed numerical methods.

2. Governing equations

Consider the deformation of an infinite, axisymmetric cylinder Ω induced by surface diffusion. The solid is periodic along the axis of symmetry, as illustrated in Fig. 1. The surface of the cylinder, denoted by its cross section in the (x,y)-plane $\mathbf{x}(\alpha,t)$, evolves to minimize the sum of the surface energy and elastic energy ([14] and references therein) through

$$\frac{\partial \mathbf{x}}{\partial t}\cdot\mathbf{n} \equiv v_n = \nabla_s^2(\beta g^{el} - \kappa), \tag{1}$$

where $\mathbf{n}$ is the unit vector normal to the surface, g^{el} is the elastic energy density, the dimensionless parameter β measures the relative strength of the elastic energy over the surface energy, and $\kappa = \nabla_s \cdot \mathbf{n}$ is the sum of the principle curvatures. Both g^{el} and β will be defined below.

The stress in the solid due to an external force with magnitude F along the x-axis, the axis of axi-symmetry, satisfies $\int_{\Omega_c} \mathbf{t}\,dA = F\mathbf{e}_1$, where Ω_c is any cross section of the solid with a plane perpendicular to x-axis, $\mathbf{t}$ is the traction and $\mathbf{e}_1 = (1,0,0)$ is the unit vector along x-axis. The solid is at mechanical equilibrium in absence of body forces, $\nabla\cdot\boldsymbol{\sigma} = \mathbf{0}$, where $\boldsymbol{\sigma}$ denotes the stress tensor. The surface of the cylinder satisfies the traction-free condition, i.e. $\mathbf{t} = \mathbf{0}$ on $\partial\Omega$. The relation between the stress and strain tensors follows Hooke's law for isotropic elasticity, i.e. $\sigma_{ij} = 2\mu\epsilon_{ij} + \lambda\epsilon_{kk}\delta_{ij}$, where μ and λ are the Lamé constants. Einstein summation notation is assumed in this study. The periodic boundary conditions require $\mathbf{u}(\mathbf{x} + L_p\mathbf{e}_1) - \mathbf{u}(\mathbf{x}) = U\mathbf{e}_1$ and $\mathbf{t}(\mathbf{x} + L_p\mathbf{e}_1) + \mathbf{t}(\mathbf{x}) = \mathbf{0}$ for any $\mathbf{x}$ in the solid, where U is a constant determined through F and L_P is the length of one period. Given F or U, the displacement $\mathbf{u}$ on the interface $\partial\Omega$ is calculated by solving the elasticity equations. Then, the elastic energy density $g^{el} = \frac{1}{2}\boldsymbol{\sigma}\cdot\boldsymbol{\epsilon}$ can be computed using a local coordinate transformation [12,27].

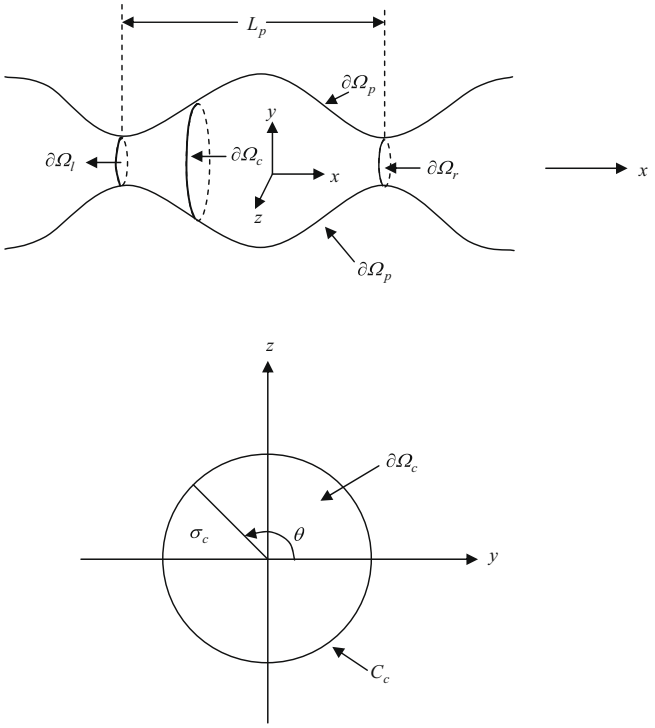

Fig. 1. Sketch of a periodic whisker.

3. Boundary integral formulation

We now derive boundary integral equations for isotropic elasticity in an axisymmetric domain which is periodic in the direction of axi-symmetry. Elastic stress arises due to an applied stress also along the direction of axi-symmetry.

Consider a volume of solid bounded by the surface $\partial\Omega$. From the Maxwell–Betti reciprocity identity, the displacement $\mathbf{u}$ and the traction $\mathbf{t}$ on the surface $\partial\Omega$ are related by the following integral equation [3]

$$\frac{1}{2}u_j(\mathbf{x}) + \oint_{\partial\Omega} u_i(\mathbf{y})\, T_{ijk}(\mathbf{y}-\mathbf{x}) n_k(\mathbf{y})\, \mathrm{d}A_{\mathbf{y}} = \int_{\partial\Omega} t_i(\mathbf{y})\, G_{ij}(\mathbf{y}-\mathbf{x})\, \mathrm{d}A_{\mathbf{y}}, \tag{2}$$

where $j = 1, 2, 3$ and $\mathbf{x}$ is a point on $\partial\Omega$. In Eq. (2), G_{ij} and T_{ijk} are the Green's functions of isotropic elasticity associated with the displacement and stress, respectively. The integral on the left-hand-side of Eq. (2) is a principal value integral.

When the solid is periodic in x-direction with a period L_p, Eq. (2) becomes [17]

$$\frac{1}{2}u_j^D(\mathbf{x}) + \oint_{\partial\Omega_p} u_i^D(\mathbf{y}) T_{ijk}^P(\mathbf{y}-\mathbf{x}) n_k(\mathbf{y})\, \mathrm{d}A_{\mathbf{y}} = -\int_{\partial\Omega_p} t_i^{(0)}(\mathbf{y}) G_{ij}^P(\mathbf{y}-\mathbf{x})\, \mathrm{d}A_{\mathbf{y}}, \tag{3}$$

where T_{ijk}^P and G_{ij}^P are the corresponding Green's functions that are L_p-periodic in x-axis. The integrals are over the surface boundary of the solid in one period, denoted by $\partial\Omega_p$. In the derivation of Eq. (3), we have decomposed the stress field $(\boldsymbol{\sigma}, \mathbf{u})$ into a uni-axial stress component, $\boldsymbol{\sigma}^{(0)} = \frac{U}{L_p}\mathrm{diag}(E, 0, 0)$ and $\mathbf{u}^{(0)} = \frac{U}{L_p}(x\mathbf{e}_1 - \nu\sigma\mathbf{e}_\sigma)$, and the disturbance field, $(\boldsymbol{\sigma}^D, \mathbf{u}^D)$ where $\mathbf{e}_\sigma$ denotes the unit vector in σ-direction of the cylindrical coordinates (x, σ, ϕ), and $E = 2\mu(1+\nu)$ is the Young's modulus. $\mathbf{t}^{(0)}$ in Eq. (3) is the corresponding traction for $\boldsymbol{\sigma}^{(0)}$. A relationship between the constants U and F takes the form

$$L_p F = \frac{U}{L_p} E V_p - 2\pi(2\mu+\lambda)\int_C u_1^D \sigma\, \mathrm{d}\sigma + 2\pi\lambda \int_C u^{D\sigma}\sigma\, \mathrm{d}x, \tag{4}$$

where V_p is the volume of the solid in one period, C is an oriented contour of the surface $\partial\Omega_p$ in (x, y)-plane in the direction of increasing x, and $\mathbf{u} = (u_1, u_\sigma, 0)$ is the displacement in the cylindrical coordinates (x, σ, ϕ). For detailed derivation of the relation (4), see [17].

Following Pozrikidis [23], due to axi-symmetry, we can integrate along ϕ-direction in the boundary integral Eq. (3) analytically and obtain

$$\frac{1}{2}u_\beta^D(\mathbf{x}) + \oint_C u_\alpha^D(\mathbf{y}) Q_{\alpha\beta\gamma}^P(\mathbf{y}-\mathbf{x}) n_\gamma(\mathbf{y})\, \mathrm{d}s_{\mathbf{y}} = -\int_C t_\alpha^{(0)}(\mathbf{y}) M_{\alpha\beta}^P(\mathbf{y}-\mathbf{x})\, \mathrm{d}s_{\mathbf{y}}, \tag{5}$$

where the indices α, β and γ take the value of x or σ in the cylindrical coordinates. $Q^P_{\alpha\beta\gamma}$ and $M^P_{\alpha\beta}$ are the corresponding one-dimensional L_p-periodic (in x-direction), axisymmetric Green's functions associated with stress and displacement, respectively. The expressions for $Q^P_{\alpha\beta\gamma}$ and $M^P_{\alpha\beta}$ are presented later in Eq. (16).

The integral Eq. (5) has one non-trivial homogeneous solution, corresponding to the rigid-body translation in the x-direction. To ensure the uniqueness of solution, following [15], we add the term $D_\alpha M^P_{\alpha\beta}(\mathbf{x})$ to the left-hand side of (5), where the vector $\mathbf{D}$ is defined as

$$D_\beta \equiv \int_C u_x(\mathbf{y}) Q^P_{x\beta\gamma}(\mathbf{y}) n_\gamma(\mathbf{y})\, ds_{\mathbf{y}}.$$

As mentioned earlier, the elastic energy density g^{el} in Eq. (1) can be obtained from the displacement $\mathbf{u}$, the solution of the integral Eq. (5), and the traction $\mathbf{t}$ on the solid surface.

4. Numerical methods

Numerical simulation of the evolution of the elastically stressed solid surface consists of two distinctive steps from algorithm design perspective: (a) solving the boundary integral equations Eq. (5) for elasticity with axi-symmetry and one-dimensional periodicity given a fixed geometry, and (b) temporal updating the highly stiff Eq. (1) for the moving interface.

4.1. Boundary integral equations for the elasticity

At each time step, in order to compute the elastic energy density g^{el} in Eq. (1), we need to solve the boundary integral equations for the elasticity, Eq. (5). In particular, the equations are for axisymmetric and one-dimensional periodic solid bodies, as depicted in Fig. 1 and the unknown is the displacement vector $\mathbf{u}$ on the boundary surface $\partial\Omega_p$. Since the axisymmetric solid surface is represented by a set of marker points on the parameterized curve $\mathbf{x}(\alpha)$ in the (x, y)-plane, the integral equations become a system of linear equations for the displacement at the marker points $\{\mathbf{u}(\mathbf{x}(\alpha_j))\}$ after discretization using the collocation method and the quadrature approximation for the integrals. The dense system of linear equations for the displacement is solved using GMRES [26]. Once the displacement and traction are known, the elastic energy density g^{el} can be computed as in [12,27]. FFT is used to calculate the derivatives of various quantities and the pseudo-spectral method is applied for the nonlinear terms (e.g. P in Eq. (26)).

4.1.1. High-order quadratures for singular and weakly-singular integrals

In this subsection, we derive and present the method for designing high-order quadratures for both single-layer and double-layer integrals appearing in Eq. (5). The high-order quadratures lead to high-order methods for solving the axisymmetric boundary integral equations. Haroldsen and Meiron [9] presented a similar method for evaluating the singular Biot–Savart integrals in doubly-periodic water wave calculation. Here, we also discuss the stability of applying the method in solving integral equations.

One of the difficulties in boundary integral method is to evaluate the singular and weakly-singular integrals in the equations with proper precisions and efficiency. In our case, the singularities of the single- and double-layer integrals in Eq. (5) are less obvious due to the complexity of the axisymmetric Green's functions as expressed in Appendix A. As the observation point $\mathbf{y}$ approaches the field point $\mathbf{x}$, the singular behavior of the Green's functions can be summarized as

$$\begin{aligned} Q^P_{\alpha\beta\gamma}(\mathbf{y}-\mathbf{x}) &= \frac{p_{\alpha\beta\gamma}}{\hat{r}} + q_{\alpha\beta\gamma}\ln\hat{r} + s_{\alpha\beta\gamma}, \\ M^P_{\alpha\beta}(\mathbf{y}-\mathbf{x}) &= u_{\alpha\beta}\ln\hat{r} + v_{\alpha\beta}, \end{aligned} \tag{6}$$

where $\hat{r} \equiv |\mathbf{y}-\mathbf{x}|$. $p_{\alpha\beta\gamma}, q_{\alpha\beta\gamma}, s_{\alpha\beta\gamma}, u_{\alpha\beta}$ and $v_{\alpha\beta}$ are smooth functions of $\mathbf{x}$ and $\mathbf{y}$ even when $\mathbf{y}\to\mathbf{x}$. Unfortunately, the expressions of these smooth functions are unknown, otherwise spectral accurate numerical integration schemes could be developed for the integrals. From the decomposition given by Eq. (6), without loss of generality, the integrals in Eq. (5) are of the form

$$I \equiv \int_{-1}^{1} g(s)\, ds = \fint_{-1}^{1} \frac{a(s)}{s}\, ds + \int_{-1}^{1} b(s)\ln|s|\, ds + \int_{-1}^{1} c(s)\, ds, \tag{7}$$

where g is a periodic function on $[-1,1]$, and a, b and c are smooth or analytic but unknown functions. The first integral on the right-hand side of Eq. (7) is taken as a Cauchy principal value integral.

Recall that the composite trapezoidal rule with uniform grid size h is spectrally accurate when applied to analytic periodic integrands. Note that the Green's functions $Q^P_{\alpha\beta\gamma}$ and $M^P_{\alpha\beta}$ are periodic functions. In absence of the log-singularity term $b(s)\ln|s|$ in the integrands, the alternating point quadrature for the integral I, defined by

$$A_h[g] = 2h \sum_{\substack{j=-n/2+1 \\ |j| \text{ odd}}}^{n/2} g(s_j), \quad \text{where } s_j = jh,\ h = 2/n, \tag{8}$$

would eliminate the error of all polynomial orders due to the Cauchy-type singularity in the regular composite trapezoidal rule, resulting in a spectrally accurate approximation to the integral (see, for example, [28]). Here, n is the number of subintervals on $[-1,1]$ and we require n be an even integer. However, in the presence of log-type singularities, the error of the quadrature is

$$E_h \equiv I - A_h[g] = -(2\log 2)b(0)h + 4\sum_{\gamma=1}^{m-1}\frac{\zeta'(-2\gamma)}{(2\gamma)!}(1-2^{2\gamma})b^{(2\gamma)}(0)h^{2\gamma+1} + O(h^{2m}), \tag{9}$$

where $\zeta(\tau)$ is the Riemann zeta function, $\zeta'(\tau) = \mathrm{d}\zeta/\mathrm{d}\tau$ and $b^{(k)}$ denotes the kth derivative of b [28].

Taking advantage of the explicit form of the quadrature error (9), one can use different approaches to construct arbitrarily high-order quadratures for evaluating the integrals of type defined in Eq. (7). One way is to find the values of the derivatives of the function b at the singular point $s = 0$ and then to modify the alternating point quadrature (8) by subtracting the leading-order error terms in Eq. (9). This method involves detailed asymptotic analysis of the integrands $Q_{\alpha\beta\gamma}$ and $M_{\alpha\beta}$, which is rather difficult and tedious if not impossible. An alternative is to use the standard Richardson extrapolation based on the alternating point quadratures (8) $A_h, A_{2h}, A_{4h}, \ldots, A_{2^{N_e}h}$ (where N_e is the number of extrapolations) for the integral (7) to eliminate the leading-order error terms without using detailed knowledge of the coefficients such as $b^{(k)}(0)$. This approach is similar to the Romberg-type quadrature but without a recursive formula for the lowest order approximations, because the starting point of the extrapolation is the alternating point quadrature instead of the standard trapezoidal rule. Although this approach is theoretically sound, we find that it is numerically unstable because the condition number of the linear system arising from discretization of the integral Eq. (5) increases as the number of marker points N_m increases. The instability is due to special structure of the coefficient matrix corresponding to the integral equation resulting from applying the extrapolations to the alternating point quadrature. If starting with the standard trapezoidal rule, the linear system obtained after applying the extrapolations would be stable.

Instead, we can obtain an arbitrarily high-order quadrature using the following approach.

- First, we remove the first-order error term in Eq. (9) of the alternating point quadrature (8) by calculating the function value $b(0)$, which is much easier compared with finding its derivatives. The resulting modified alternating point quadrature is

$$MA_h[g] = -(2\log 2)b(0)h + 2h\sum_{\substack{j=-n/2+1\\ |j| \text{ odd}}}^{n/2} g(s_j). \tag{10}$$

  The error expansion for (10) contains every term with odd-power of h except the term that is linear in h.
- Second, we apply Richardson extrapolation on the modified alternating point quadrature (10) based on the principle that only the existing quadrature points are used in the extrapolation process.

For examples, the fifth- and seventh-order quadratures can be derived as following:

Fifth-order quadrature: Following the above two steps and working with the modified alternating point quadratures $MA_h[g]$ and $MA_{3h}[g]$, we obtain the fifth-order quadrature rule for the integral (7)

$$R_1(h) = \sum_{\substack{j=-n/2+1\\ |j| \text{ odd}}}^{n/2} g(s_j)h_j - (\log 2)b(0)F_A h, \tag{11}$$

where

$$h_j = \begin{cases} F_A h := \frac{24}{13}h, & \text{if } |j| \text{ is a multiple of 3,} \\ F_B h := \frac{27}{13}h, & \text{if } |j| \text{ otherwise.} \end{cases} \tag{12}$$

Seventh-order quadrature: Similarly, based on the modified alternating point quadratures $MA_h[g], MA_{3h}[g]$ and $MA_{5h}[g]$, we have the seventh-order quadrature

$$R_2(h) = \sum_{\substack{j=-n/2+1\\ |j| \text{ odd}}}^{n/2} g(s_j)h_j - (\log 2)b(0)F_C h, \tag{13}$$

where

$$h_j = \begin{cases} F_C h := \frac{1920}{1067}h, & \text{if } |j| \text{ is a multiple of 3 and 5,} \\ F_D h := \frac{1875}{1067}h, & \text{if } |j| \text{ is a multiple of 3 not 5,} \\ F_E h := \frac{2295}{1067}h, & \text{if } |j| \text{ is a multiple of 5 not 3,} \\ F_F h := \frac{2250}{1067}h, & \text{if } |j| \text{ otherwise.} \end{cases} \tag{14}$$

Next, we demonstrate the order of convergence for solving the elasticity equations Eq. (5) when the seventh-order modified Romberg-type quadrature (13) is used. We compare the numerical solution of Eq. (2) with the exact solution for an axisymmetric infinite rod, which is 2π-periodic in x-direction, for the applied plane stress $\boldsymbol{\sigma} = \mathrm{diag}(2\lambda, 2(\mu+\lambda), 2(\mu+\lambda))$ given in Cartesian coordinates. The analytic solution for the displacement is $\mathbf{u}_{\mathrm{exact}} = \sigma \mathbf{e}_\sigma$ for any shape profile of the cylindrical rod $\sigma = \sigma(\alpha)$. The shape used in the test is given by $x(\alpha) = \alpha, \sigma(\alpha) = 1 + (\sin\alpha + \cos\alpha)/3$.

Table 1 shows the maximum error in the displacement, $\mathrm{err}_{\mathbf{u}}(N_m) := \max_{1\leqslant j\leqslant N_m} |\mathbf{u}_j - \mathbf{u}_{\mathrm{exact}}(\alpha_j)|$, for different values of the total marker points N_m on the interface. In the computations, the GMRES tolerance level is set at 10^{-13}. Our direct simulation clearly shows the order of accuracy, seven, as expected in theory. The numerical order of convergence in the table is obtained by computing $\log_2(\mathrm{err}_{\mathbf{u}}(N_m)/\mathrm{err}_{\mathbf{u}}(2N_m))$. For the seventh-order quadrature (13), the number of marker points N_m must be multiples of 30 because it has to be even and can be divided by 3 and 5.

4.1.2. Fast summations for one-dimensional periodic, axisymmetric Green's functions

It is well known that, without using fast algorithms (such as fast multipole method) for solving the integral equations, almost the entire computational cost is spent on evaluating the Green's functions. Efficient and accurate evaluation of the kernels is indispensable in boundary integral methods.

The boundary integral formulation described in this study requires evaluating the axisymmetric Green's functions $Q^P_{\alpha\beta\gamma}$ and $M^P_{\alpha\beta}$ that are periodic in the axial direction (x-direction) with a period L_p. Furthermore, the accuracy of numerical integration presented earlier relies on the assumption that the integrands are periodic. If the integrand g in (7) is not periodic, then the quadrature error given in (9) must be modified as [28]

$$E_h = -(2\log 2)b(0)h + 4\sum_{\gamma=1}^{m-1} \frac{\zeta'(-2\gamma)}{(2\gamma)!}(1-2^{2\gamma})b^{(2\gamma)}(0)h^{2\gamma+1} + 2\sum_{\gamma=1}^{m-1} \frac{B_{2\gamma}}{(2\gamma)!}(1-2^{2\gamma-1})[g^{(2\gamma)}(-1) - g^{(2\gamma)}(1)]h^{2\gamma} + O(h^{2m}), \tag{15}$$

where B_γ are the Bernoulli numbers.

The difficulty in constructing an efficient method for evaluating the periodic Green's functions is the complex expressions corresponding to the free-space axisymmetric ones expressed in Eqs. (33) and (35) (given in the Appendix A). The one-dimensional L_p-periodic, axisymmetric Greens functions can be obtained from direct summation of the non-periodic axisymmetric ones,

$$M^P_{\alpha\beta}(\mathbf{y}-\mathbf{x}) = \sum_{l=-\infty}^{\infty} M_{\alpha\beta}(\mathbf{y}-\mathbf{x}-lL_p\mathbf{e}_1), \quad Q^P_{\alpha\beta\gamma}(\mathbf{y}-\mathbf{x}) = \sum_{l=-\infty}^{\infty} Q_{\alpha\beta\gamma}(\mathbf{y}-\mathbf{x}-lL_p\mathbf{e}_1). \tag{16}$$

The popular Ewald summation technique (see [24] and references therein) cannot be applied here. Here we present a fast summation method based on the asymptotic analysis of the truncated sums in the singly-periodic functions (16), denoted by

$$M^{n_p}_{\alpha\beta} = \sum_{l=-n_p}^{n_p} M_{\alpha\beta}(\mathbf{y}-\mathbf{x}-lL_p\mathbf{e}_1), \quad Q^{n_p}_{\alpha\beta\gamma} = \sum_{l=-n_p}^{n_p} Q_{\alpha\beta\gamma}(\mathbf{y}-\mathbf{x}-lL_p\mathbf{e}_1). \tag{17}$$

An alternative fast method for periodic structure is based on the fast multipole method [16].

First, we note that all the infinite sums in (16) are convergent except the component M^P_{xx}. Since the definition of Green's function allows us to add an arbitrary constant, in our computation, we modify the expression of M^P_{xx} by

$$M^P_{xx}(\mathbf{y}-\mathbf{x}) = \sum_{l=-\infty}^{\infty} \left[M_{\alpha\beta}(\mathbf{y}-\mathbf{x}-lL_p\mathbf{e}_1) - \frac{\sigma_y}{2L_p\mu}\frac{1}{|l|} \right]. \tag{18}$$

Analyzing the decay rate of $M_{\alpha\beta}$ and $Q_{\alpha\beta\gamma}$ for large arguments $|\mathbf{y}-\mathbf{x}|$, we find that the truncation errors of replacing the infinite sums (16) by the summations of over finite number of periods (17) can be represented by

$$E_G(n_p) = \frac{C_1}{n_p^2} + \frac{C_2}{n_p^3} + \cdots, \tag{19}$$

where C_i's are functions of $\mathbf{y}-\mathbf{x}$.

Now, we can apply Richardson extrapolation technique to obtain an efficient and accurate method for evaluating the periodic Green's functions. Define

Table 1
Convergence of the elasticity solver based on a seventh-order quadrature. $\mathrm{err}_{\mathbf{u}}$ is the maximum error in the displacement $\mathbf{u}$ defined by $\mathrm{err}_{\mathbf{u}} := \max_{1\leqslant j\leqslant N_m} |\mathbf{u}_j - \mathbf{u}_{\mathrm{exact}}(\alpha_j)|$; N_m is the total number of points on the interface.

N_m	30	60	120	240	480
$\mathrm{err}_{\mathbf{u}}$	2.0×10^{-3}	8.3×10^{-5}	1.0×10^{-6}	5.5×10^{-9}	3.9×10^{-11}
Order		4.6	6.3	7.5	7.1

$$S(i,0) = \sum_{l=-2^i}^{2^i} G(\mathbf{y} - \mathbf{x} - L_p l \mathbf{e}_1), \tag{20}$$

where G stands for one of the components in $M_{\alpha\beta}$ and $Q_{\alpha\beta\gamma}$. The Richardson extrapolation procedure can be presented as

$$\begin{aligned} S(0,0) &= \sum_{l=-1}^{1} G(\mathbf{y} - \mathbf{x} - L_p l \mathbf{e}_1), \\ S(i,0) &= S(i-1,0) + \sum_{2^{i-1}+1 \leqslant |l| \leqslant 2^i} G(\mathbf{y} - \mathbf{x} - L_p l \mathbf{e}_1), \quad \text{for } i = 1,2,\ldots,N_g, \\ S(i,j) &= S(i,j-1) + \frac{1}{2^{j+1}-1}[S(i,j-1) - S(i-1,j-1)], \quad \text{for } i = j, j+1, \ldots, N_g;\ j = 1,2,\ldots,N_g. \end{aligned} \tag{21}$$

Here N_g is the number of Richardson extrapolations.

To demonstrate the effect of Richardson extrapolation, we measure the maximum errors in Green's function evaluation during the numerical integration in solving the boundary integral Eq. (5) for the cylindrical profile $x(\alpha) = \alpha$, $\sigma(\alpha) = 1 + (\sin\alpha + \cos\alpha)/3$. Table 2 compares the errors in evaluating different components of the Green's functions using the new extrapolation strategy and the direct summation. We regard the function values obtained from $S(8,8)$ as the exact values, as the difference between $S(7,7)$ and $S(8,8)$ are at least two orders smaller than the numbers shown in Table 2. The errors in the function evaluation are about four orders of magnitude smaller when we use the extrapolation formula given in (21) with $N_g = 5$ (the row in the table labeled by $S(5,5)$), comparing to those of the direction summation $S(5,0)$. In order to achieve similar accuracy of $S(5,5)$ which covers 65 periods, without the extrapolation, one would have to sum over more than 8193 periods (see the row labeled by $S(11,0)$). It is important to note the extrapolation costs effectively no computational time because it involves a few floating-point additions, subtractions and division by integers.

By choosing $N_g \geqslant 5$, we find that the numerical solutions to the integral Eq. (5) are indistinguishable for our choice of the tolerance in GMRES solver. The numerical results presented in this paper are obtained by setting $N_g = 5$.

4.2. Time integration

Detailed discussions of a second-order time integration schemes that reduce the time-step constraint are given in our previous study [17]. Here, we summarize the steps for completeness and present a new fourth-order method based on the integration factor techniques and the Runge–Kutta method. Similar technique of removing stiffness in time integration have been applied in previous studies of stressed solids, e.g., for Ostwald ripening of two-dimensional particles [33] and for evolution of voids with anisotropic surface energy [29].

We evolve the solid surface $C, x(\alpha,t)\mathbf{e}_1 + \sigma(\alpha,t)\mathbf{e}_\sigma$, by advancing the pair of local geometrical variables (s_α, θ), where s_α and θ are the local arc-length derivative and the tangent angle, respectively. The relation between the two equivalent sets of variables is given by $(x_\alpha, \sigma_\alpha)/s_\alpha = (\cos\theta(\alpha,t), \sin\theta(\alpha,t))$. The differential equations for (s_α, θ) are

$$s_{\alpha t} = T_\alpha - \theta_\alpha v_n, \tag{22}$$

$$\theta_t = \frac{v_{n\alpha} + T\theta_\alpha}{s_\alpha}, \tag{23}$$

where T is the tangential velocity specified by

$$T(\alpha,t) = -\frac{\alpha}{2\pi}\int_0^{2\pi} \theta_{\alpha'} v_n \,\mathrm{d}\alpha' + \int_0^{\alpha} \theta_{\alpha'} v_n \,\mathrm{d}\alpha'. \tag{24}$$

This choice of tangential velocity keeps s_α constant in space satisfying $s_\alpha(\alpha,t) = L(t)/2\pi$, where L is the total arc-length of C. In other words, the marker points are evenly distributed along the interface at any instant. Accordingly, the Eq. (22) for s_α is replaced by

$$L_t = -\int_0^{2\pi} \theta_{\alpha'} v_n \,\mathrm{d}\alpha'. \tag{25}$$

Table 2
Effect of extrapolation in Green's function evaluation. The table shows the maximum error in evaluating the different components of the Green's functions, where M^P_{*x} includes M^P_{xx} and $M^P_{\sigma x}$ and similarly for the other entries. $S(i,0)$ is the direct summation over $2^{i+1}+1$ periods defined in Eq. (20), and $S(i,i)$ is the result of extrapolating i times the values in $S(i,0)$ as defined in Eq. (21).

	M^P_{*x}	$M^P_{*\sigma}$	Q^P_{*x*}	$Q^P_{*\sigma*}$
$S(5,0)$	2.1×10^{-5}	3.1×10^{-6}	9.6×10^{-5}	2.5×10^{-6}
$S(5,5)$	1.0×10^{-9}	8.8×10^{-11}	1.5×10^{-9}	3.4×10^{-10}
$S(11,0)$	1.4×10^{-9}	6.9×10^{-10}	2.6×10^{-9}	3.2×10^{-9}

The equation for the normal velocity v_n, Eq. (1), can be decomposed as $v_n = -\theta_{sss} + P$, where

$$P = -\frac{\sigma_s}{\sigma}\frac{\partial \kappa_{2d}}{\partial s} + \nabla_s^2(-\kappa_\infty + \beta g^{el}). \tag{26}$$

Note that the curvature $\kappa = \kappa_{2d} + \kappa_\infty$, where $\kappa_{2d} = \theta_s$ and $\kappa_\infty = -\cos\theta/\sigma$ are the curvatures in the meridian and azimuthal directions, respectively, and the surface Laplacian in axisymmetric geometry is given by

$$\nabla_s^2 = \frac{\partial^2}{\partial s^2} + \frac{\sigma_s}{\sigma}\frac{\partial}{\partial s}. \tag{27}$$

Substituting the expression of v_n into Eq. (23), the evolution of θ becomes

$$\theta_t = -\theta_{ssss} + (P_s + T\theta_s). \tag{28}$$

The temporal stability constraint of an explicit time integration scheme is dictated by the term with the highest order of derivative. Therefore, a standard explicit scheme, such as Runge–Kutta methods or linear multi-step type methods, applied to Eq. (28) requires a time-step proportional to $(\Delta s)^4$, where Δs is the mesh size. On the other hand, a fully implicit temporal scheme on Eq. (28) leads to nonlinear systems that have to be solved at every time-step. For both approaches, the computational costs are very expensive, and become prohibitive for medium to small mesh sizes.

Realizing that the fourth-order derivative term is linear and diagonalized in Fourier space, we rewrite Eq. (28) in Fourier space and obtain the equations for the corresponding Fourier coefficients of θ

$$\hat{\theta}_t(k) = -f(k,t)\hat{\theta}(k) + \widehat{A}(k), \tag{29}$$

where $f(k,t) \equiv (2\pi/L(t))^4 k^4$, $\widehat{A}(k)$ is the Fourier coefficient for $P_s + T\theta_s$ and k denotes the wavenumber. Then, we treat the $k^4\hat{\theta}(k)$ term with the integration factor technique and the nonlinear term explicitly such that the stability constraint associated with the fourth-order derivative term is removed without the need of solving any nonlinear systems.

In particular, because the interfaces might develop singularities, in order to achieve high accuracy, we derive a fourth-order scheme based on the classical explicit Runge–Kutta method. We point out that the technique can be applied to any equations can be written in the form of Eq. (29) with arbitrary $f(k,t)$.

Define $\psi(k,t) = \exp(\int_0^t f(k,t')\mathrm{d}t')\hat{\theta}(k,t)$. Using integration factor method on Eq. (29), the governing equation for $\psi(k,t)$ becomes

$$\psi_t = g(t,\psi) \equiv \exp\left(\int_0^t f(k,t')\,\mathrm{d}t'\right)\widehat{A}(k). \tag{30}$$

Applying the fourth-order Runge–Kutta method to Eq. (30), we obtain

$$\hat{\theta}^{n+1} = e_k(t_n,t_{n+1})\hat{\theta}^n + \frac{\Delta t}{6}\left[e_k(t_n,t_{n+1})\widehat{A}^n + 2e_k\left(t_{n+\frac{1}{2}},t_{n+1}\right)\left(\widehat{A}^{n+\frac{1}{2}} + \widehat{A}^{n+\frac{1}{2}*}\right) + \widehat{A}^{n+1*}\right], \tag{31}$$

where $e_k(a,b) \equiv \exp(-\int_a^b f(k,t')\,\mathrm{d}t')$, $t_n = n\Delta t$, and $\widehat{A}^n$ denotes $\widehat{A}(k)$ at time t_n. The terms $\widehat{A}^{n+\frac{1}{2}}$, $\widehat{A}^{n+\frac{1}{2}*}$ and $\widehat{A}^{n+1*}$ correspond to $\hat{\theta}^{n+\frac{1}{2}}$, $\hat{\theta}^{n+\frac{1}{2}*}$ and $\hat{\theta}^{n+1*}$, respectively, and they are obtained by

$$\begin{aligned}
\hat{\theta}^{n+\frac{1}{2}} &= e_k\left(t_n,t_{n+\frac{1}{2}}\right)\left[\hat{\theta}^n + \frac{\Delta t}{2}\widehat{A}^n\right],\\
\hat{\theta}^{n+\frac{1}{2}*} &= e_k\left(t_n,t_{n+\frac{1}{2}}\right)\hat{\theta}^n + \frac{\Delta t}{2}\widehat{A}^{n+\frac{1}{2}},\\
\hat{\theta}^{n+1*} &= e_k(t_n,t_{n+1})\hat{\theta}^n + \Delta t e_k\left(t_{n+\frac{1}{2}},t_{n+1}\right)\widehat{A}^{n+\frac{1}{2}*}.
\end{aligned} \tag{32}$$

It is well known that the time-stepping methods in Fourier space have aliasing errors due to the high-order derivatives, and the small-scale numerical oscillation is usually controlled by using Fourier filtering to damp the highest modes [10]. We find that the artificial Fourier filtering is not necessary in our case, because the multipliers $e_k(a,b)$ appearing in the schemes (31) and (32) provide enough damping to high-frequency terms. Note that e_k decays to zero in $O(\exp(-k^4))$ as the wavenumber k increases.

5. Numerical results

The dimensionless parameter that characterizes the dynamics of the whisker is given by $\beta \equiv R_0 E\tilde{\epsilon}^2/\gamma$, which measures the relative strength of the elastic energy compared with the surface energy. The non-dimensionalization is done by choosing the radius of the undisturbed cylinder R_0 as the length scale, $\tilde{\epsilon} = U_1/R_0$ and $E\tilde{\epsilon}$ as the scales of the strain and stress, respectively, and $R_0^4 k_T/(D_s\gamma V_a^2 A_0)$ as the time scale, where D_s is the surface diffusivity coefficient, V_a is the atomic volume, A_0 is the number of atoms per unit area on the interface, and k_T is the thermal energy. Note E is Young's modulus and γ is the solid-vapor surface tension.

Our previous work [17] has validated the numerical implementation by comparing the numerical results with those from the linear analysis on small perturbation, even though it used less accurate schemes for solving the elasticity equations and

advancing in time. We have repeated the validation using the numerical methods presented in this work and the results agree with that of the linear theory well as in [17]. Next, we focus on presenting a numerical result that would have been impossible to obtain using less accurate schemes, such as in [17]. In particular, we study the existence and the form of finite-time singularity developed on the solid surface.

5.1. Without elasticity ($\beta = 0$)

In absence of the applied stress, $\beta = 0$, evolution of the cylindrical surface with axisymmetric disturbances has been studied intensively (see [2] and references therein). In this case, the surface diffusion drives unstable long-wave disturbances toward a finite-time pinchoff. Furthermore, it has been shown that the pinchoff is self-similar and the cylinder forms a cone with half-cone angle of 46.0444° when it collapses onto the axis of symmetry.

Because of the accurate schemes developed in this work, we are able to show the formation of singularity and, furthermore, that the predicted cone angle matches well with the results in previous work, based on our direct numerical simulation of the original fully nonlinear Eq. (1).

In Fig. 2(a), we show a sequence of the solid surface profiles during the evolution. The initial shape is a sinusoidal perturbation of a straight cylindrical cylinder, given by $\sigma(x) = 1 + 0.1\cos(x/\sqrt{2})$. The result clearly shows the cylinder pinches and the surface develops sharp curvatures at the minimum neck width. In our simulation, in order to save computational time, we start with 64 marker points ($N_m = 64$) and double the number of marker points whenever the evenly distributed points are not enough to resolve the high curvature area of the shape configurations. The inadequacy of the resolution can be also detected from the loss of conservation of the volume of the numerical solution. We double the number of marker points N_m when the relative change in the volume of the rod is larger than 10^{-7} comparing with the volume at the start. For the numerical results in Fig. 2, $N_m = 1024$ near the end of pinchoff.

To investigate whether a geometrical singularity develops and the form of the singularity (a cusp, a corner or other types of singularity), one needs to apply data fitting and extrapolation techniques based on the full simulation data close to the time of singularity formation. In Fig. 2(b)–(d), we plot the reciprocal of maximum plane curvature of the trace of the cylinder in the (x, y)-plane, $1/\max\kappa_{2d}$, the minimum neck width, and the half-cone angle near the pinchoff point as functions of time t. The numerical data are shown by the circular marks in the graphs. The dashed lines in the figures are the polynomials of degree two interpolating the last three data points (i.e., the numerical data at the times closest to the singularity formation time). Fig. 2(b) shows that the extrapolation from the interpolating polynomial predicts the curvature blows up, equivalently the singularity forms, at the estimated singularity time $t_c = 4.53242$. Using the interpolating polynomial for the minimum neck width based on the same three data sets, we obtain the extrapolated value of minimum neck width is 0.00326 at the singularity time t_c estimated from the curvature data. Theoretically, the cylinder forms cone as it collapse onto the axis of

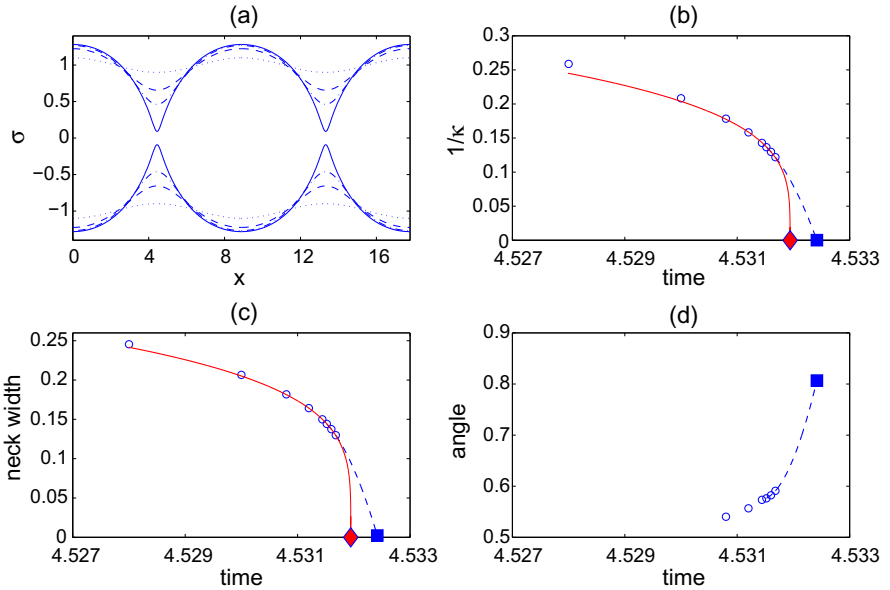

Fig. 2. (a) A sequence of surface profiles for $\beta = 0$ at times $t = 0$ (the dotted line), 3.6 (the dashed line), 4.32 (the dash-dotted line) and 4.53168 (the solid line). (b) The reciprocal of the maximum plane curvature for the cylinder against the time, where the numerical results are indicated with the circles (o's) and the nonlinear least square form fit and quadratic polynomial interpolation and extrapolation are shown in solid and dashed lines, respectively. The solid diamond and square symbols are the singularity times where the maximum curvature is infinity, predicted by the least square and polynomial fits, respectively. (c) Same as (b) except that the minimum neck width is plotted. (d) Same as (b) except that the half-cone angle is plotted. The square symbol predicts the value of the angle at the estimated singularity time from the polynomial fit.

symmetry, i.e., the curvature becomes infinity as the minimum neck width reaches zero. Considering the interface is represented by 1024 marker points, our extrapolated value of the neck width at the estimated time when the curvature blows up, 0.00326, is rather accurate. Furthermore, the polynomial extrapolation from the cone angle data predicts the half-cone angle would be 0.8067 in radian or 46.22° at the time t_c, which differs from the accurate estimate 46.0444° obtained from similarity solution by 0.4%.

In this case, we know the pinchoff process is self-similar, e.g. [2]. We also have performed the nonlinear least square fit of the form $A^*(T_c - t)^p$ based on the last six data points in both Fig. 2(b) and (c). The least square fit from the curvature data, plotted using the solid line in Fig. 2(b), predicts the singularity time $T_c = 4.53194$ and the power $p = 0.2595$. The form fit from the minimum neck width data predicts $T_c = 4.53195$ and $p = 0.2317$, shown with the solid line in Fig. 2(c). The results from the least square fit are consistent in predicting the singularity time and the values of p are also close to the theoretical value $1/4$. Although the predicted values of the singularity time from the form fit T_c are slightly less than the one predicted from the polynomial fit t_c, the quadratic polynomial fit can be considered as a truncated Taylor expansion of the curvature and minimum neck width near the singularity time. Because the form of the cone angle near the pinchoff is unknown, we did not analyze the cone angle data using form fitting.

The consistency of the result is further checked by using $N_m = 4096$ marker points and applying the same polynomial interpolation and extrapolation techniques as above. For this numerical resolution, we obtain the estimated minimum neck width at the singularity time, predicted by the blow-up of the plane curvature, is accurate to the fourth digit. In addition, we have used other data points near the end of simulation to perform the polynomial extrapolation and obtained almost the same results. Therefore, we simulate with $N_m = 1024$ marker points in the numerical study of stressed solid surface diffusion, presented in the next section.

The consistency of our numerical results and the agreement with previous similarity solution [2] suggest that our numerical methods are accurate for predicting singularity formation and exploring the singularity types. Importantly, we will use the exactly same numerical methods including the polynomial interpolation and extrapolation procedures in the unexplored stressed-solid case, discussed in the next subsection.

5.2. With elasticity ($\beta > 0$)

In the presence of the elastic stress $\beta > 0$, we will show that the whisker does not collapse onto the axis but forms a finite-time singularity (a corner), starting with a perturbed cylinder. This result is in contrast with that of stress-driven instability in a two-dimensional semi-infinite solid where numerical evidence of cusp formation is shown by Spencer and Meiron [31].

Our formulation of the applied stress on the whisker agrees with that in the linear studies [5,14] up to the leading order. The linear analysis of Kirill et al. [14] shows that, for the Poisson ratio $\nu = \frac{1}{3}$ and the elastic parameter $\beta = 0.01$, the most linearly unstable sinusoidal perturbation to the cylindrical whisker has the wavenumber very close to that of $\beta = 0 : k = \frac{1}{\sqrt{2}}$. We choose the initial configuration to be the straight cylinder perturbed by this sinusoidal wave: $\sigma = 1 + 0.1\cos(kx)$ with $k = \frac{1}{\sqrt{2}}$.

To save computational time, we start the simulation with 120 number of marker points on the interface, i.e. $N_m = 120$. We increase the spatial resolution by doubling the number of marker points N_m when the resolution is not adequate to represent the section of sharp curvature. We apply the following rule in determining when to double the number of points: (a) when

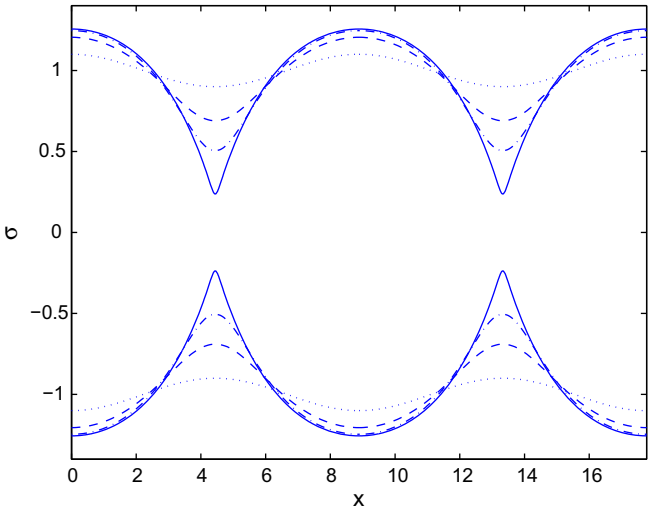

Fig. 3. Evolution of a cylindrical whisker using the initial profile $\sigma = 1 + 0.1\cos(kx)$ with the wavenumber $k = \frac{1}{\sqrt{2}}$ (shown by the dotted line) and $\beta = 0.01$. The cross sections in the (x, y)-plane of the whisker are shown at the nondimensionalized time $t = 3$ (the dashed line), 3.7 (the dash-dotted line), and 3.85672 (the solid line).

the change in the volume of the solid is greater than 0.01% of the original volume; or (b) when the change of the maximum curvature of the interface is larger than 0.1% after we double the number of marker points. In this case, the resolution is 960 marker points at the end of simulation.

The size of time-step Δt in the simulation is chosen to satisfy both the stability and accuracy constraints. Initially, $\Delta t = 8 \times 10^{-4}$ for $N_m = 120$. To satisfy the stability condition alone, we need to reduce Δt by a factor of six when N_m is doubled. The factor would be sixteen if the stiffness of surface diffusion were not treated such as by the integration factor method with a fourth-order Runge–Kutta presented in Section 4.2. Because the shape develops a singularity in finite time, the dynamics become faster when it is close to the singularity time. In our simulation, to achieve high accuracy, we reduce the time-step Δt by a factor about ten when doubling N_m, controlling the local truncation error in time integration method. Near the end of the simulation, the time-step size is 4×10^{-7} while $N_m = 960$.

Fig. 3 displays the shape evolution of the whisker at times $t = 3, 3.7$ and 3.85672, where two periods of the periodic cylinder are shown (the period in x-direction is $2\sqrt{2}\pi$ in this case). The corresponding dimensionless parameters in the simulation are $v = \frac{1}{3}$ and $\beta = 0.01$. The numerical results show that the neck of the whisker shrinks and the width increases where the whisker bulges initially. At later stages of the evolution, the whisker changes shape at a much faster pace near the section of small neck width than the other sections of the cylinder. As we will show below, the whisker develops a corner in finite time at the points of the minimum neck width, $x_c = (2m+1)\sqrt{2}\pi$ where m is an integer.

In order to show that the whisker develops a finite-time singularity before it collapses onto the axis of symmetry, we plot the reciprocal of the maximum plane curvature of the trace of the cylinder in the (x, y)-plane, $1/\max \kappa_{2d}$, and the minimum neck width against time t as functions of time t in Fig. 4(b) and (c). The full simulation data, shown by the circular marks in the graphs, are chosen at times close to the singularity formation, and the quadratic polynomial interpolation using the last three data points are also shown by the dashed lines in the figures. Extrapolating the data based the polynomials, we estimate that the critical time that the singularity forms, i.e. the time that the plane curvature blows up, is approximately $t_c = 3.85712$. At the critical time, the minimum neck width is about 0.289, which is far away from zero, and much larger than the grid size on the interface ($N_m = 960$ in this case). Fig. 4(c) suggests that the rate of neck thinning is finite as the corner forms. Our boundary integral method breaks down as a geometrical singularity forms and our results cannot predict the behavior of the evolution beyond the singularity formation. Again, note that we have used the same numerical procedure and the exactly same polynomial interpolation and extrapolation as in the case of no applied elastic stress $\beta = 0$ with $N_m = 1024$.

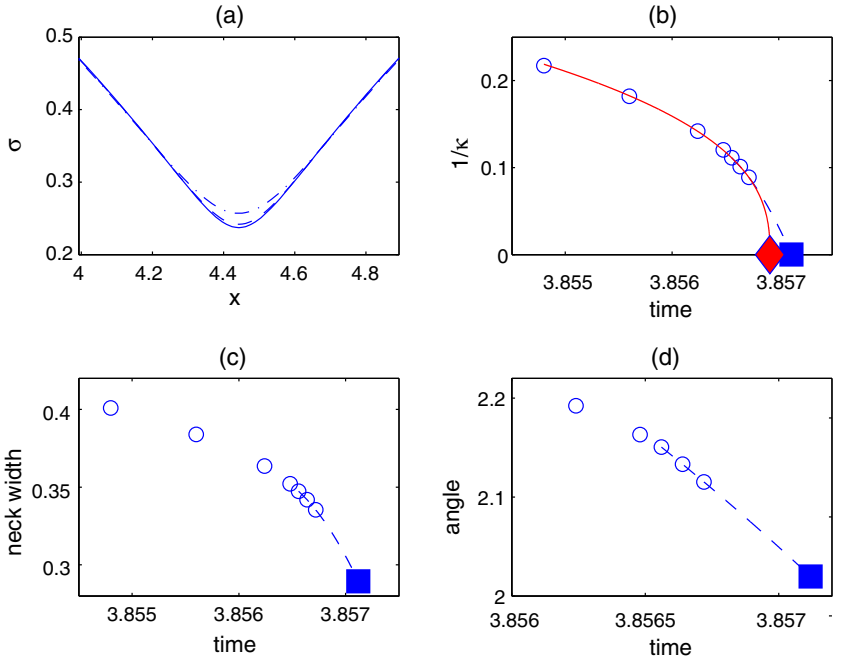

Fig. 4. (a) The close-up of the snapshots near the singularity at times $t = 3.8562$ (the dash-dotted line), 3.85664 (the dashed line) and 3.85672 (the solid line). (b) The reciprocal of the maximum plane curvature for the cylinder against the time, where the full simulation data are indicated with the circles (o's) and the polynomial fit and the nonlinear least square form fit are shown in dashed and solid lines, respectively. The solid square and diamond symbols are the singularity times where the maximum curvature is infinity, estimated from the polynomial fit and the least square form fit, respectively. (c) Same as (b) except that the minimum neck width is plotted. The square symbol indicates the extrapolated value of the minimum neck width at the estimated singularity time from the polynomial fit. (d) Data points in (a) are used for the angle of the corner. The square symbol predicts the value of the angle at the estimated singularity time from the polynomial fit.

Since there is no known self-similar theory for this case, we present only the form fitting for the data $1/\max \kappa_{2d}$ shown in Fig. 4(b). Assuming the form of $A(T_c - t)^p$ as before, the nonlinear least square fit predicts the singularity time $T_c = 3.85692$ shown with the solid line in Fig. 4(b) and the power $p = 0.3805$. Since the value of the singularity time estimated from the form fitting T_c is smaller than that from polynomial extrapolation t_c, the result suggests that minimum neck width remain nonzero when the surface develops the geometric singularity. Although the estimated singularity times are different from the different data fitting methods, the qualitative conclusion on whether the solid pinches off are consistent.

Next, we show the solid surface forms a corner instead of other types of singularities. Fig. 4(a) displays a series of close-up snapshots near the point x_c where the singularity forms. The plots suggest that the trace of the cylinder in the (x, y)-plane develops a corner at x_c. We estimate the angle of the corner as follows. We first measure the angle of rounded corner by fitting straight lines nearby but away from the tip of the corner x_c at times close to singularity formation, as shown by the circular symbols in Fig. 4(d). Then, we fit a polynomial of degree two using these angles (shown as the solid line in Fig. 4(d)) and extrapolate at the estimated singularity time $t_c = 3.85712$ (shown as the dashed line and the square symbol). The predicted value of the corner angle is about 2.02 in radian or 116°, based on the same numerical procedures used for the case of absence of elasticity $\beta = 0$.

5.3. Conclusions

In this study, we have presented an extrapolation method along with a modified alternating point quadrature for developing high-order boundary integral methods in axisymmetric domains. Although the method has been applied to solving the axisymmetric elasticity system, it can be extended to other systems where boundary integral techniques are applicable, for instance, interfacial systems in Stokes flows.

We also have presented a new method for accelerating the slowly convergent infinite series for calculation of the periodic Green's functions. The computational cost in evaluating Green's functions usually is dominant in the overall cost of a boundary integral method, especially for axisymmetric domains and periodic configurations. Further investigation on devising faster algorithms for calculating the complicated Green's functions is warranted.

We have employed the developed high-order and efficient numerical methods to study the singularity formation due to surface diffusion. It is important to note that the full nonlinear evolution equation is simulated in this study without assumptions on the form of solution, except restricting the interface to be the axisymmetric. In absence of stress, the methods are capable of reproducing the well-known pinchoff of the cylinder, and predicting accurately the form of the singularity, i.e. the cone formation at the point of pinchoff. With the applied uni-axial stress, we have found that the cylinder forms a corner before it collapses onto the axis of symmetry. It would be interesting to further investigate the dependence of the corner angle on the relative magnitude of applied stress.

Acknowledgments

The work was partially supported by NSF DMS-0511411 (X.L.) and NSF DMS-0511169 (Q.N.). This material was based upon work partially supported by the National Science Foundation under Grant DMS-0635449 to the Statistical and Applied Mathematical Sciences Institute. Any opinions, findings, and conclusions or recommendations expressed in this material are those of the authors and do not necessarily reflect the views of the National Science Foundation.

Appendix A. Axisymmetric Green's functions

We obtain the axisymmetric Green's functions $Q_{\alpha\beta\gamma}$ and $M_{\alpha\beta}$ by integrating the free-space Green's functions for isotropic elasticity with respect to the polar angle ϕ. For the points $\mathbf{x} = (x_1, \sigma_x, 0)$ and $\mathbf{y} = (y_1, \sigma_y, 0)$ in cylindrical coordinates, the axisymmetric Green's functions associated with displacement are given by

$$\begin{aligned}
M_{xx}(\mathbf{y}-\mathbf{x}) &= \frac{\sigma_y}{16\pi\mu(1-\nu)}[(3-4\nu)I_{10} + \hat{x}^2 I_{30}],\\
M_{x\sigma}(\mathbf{y}-\mathbf{x}) &= \frac{\sigma_y \hat{x}}{16\pi\mu(1-\nu)}[\sigma_y I_{31} - \sigma_x I_{30}],\\
M_{\sigma x}(\mathbf{y}-\mathbf{x}) &= \frac{\sigma_y \hat{x}}{16\pi\mu(1-\nu)}[\sigma_y I_{30} - \sigma_x I_{31}],\\
M_{\sigma\sigma}(\mathbf{y}-\mathbf{x}) &= \frac{\sigma_y}{16\pi\mu(1-\nu)}[(3-4\nu)I_{11} + (\sigma_y^2+\sigma_x^2)I_{31} - \sigma_y\sigma_x(I_{30}+I_{32})],
\end{aligned} \tag{33}$$

where $\hat{x} = y_1 - x_1$ and the integrals I_{mn} are defined by

$$I_{mn}(\hat{x}, \sigma_y, \sigma_x) = \int_0^{2\pi} \frac{\cos^n \phi}{[\hat{x}^2 + \sigma_y^2 + \sigma_x^2 - 2\sigma_y\sigma_x \cos\phi]^{m/2}} \mathrm{d}\phi. \tag{34}$$

The integrals I_{mn} can be expressed in terms of complete elliptic integrals of the first and second kind [7]. The corresponding axisymmetric Green's functions associated with stress are given by

$$
\begin{aligned}
Q_{xxx}(\mathbf{y}-\mathbf{x}) &= -\frac{\sigma_y \hat{x}}{8\pi(1-\nu)}[(1-2\nu)I_{30}+3\hat{x}^2 I_{50}],\\
Q_{xx\sigma}(\mathbf{y}-\mathbf{x}) &= -\frac{\sigma_y}{8\pi(1-\nu)}[(1-2\nu)(\sigma_y I_{30}-\sigma_x I_{31})+3\hat{x}^2(\sigma_y I_{50}-\sigma_x I_{51})],\\
Q_{x\sigma x}(\mathbf{y}-\mathbf{x}) &= -\frac{\sigma_y}{8\pi(1-\nu)}[-(1-2\nu)(\sigma_y I_{31}-\sigma_x I_{30})+3\hat{x}^2(\sigma_y I_{51}-\sigma_x I_{50})],\\
Q_{x\sigma\sigma}(\mathbf{y}-\mathbf{x}) &= -\frac{\sigma_y \hat{x}}{8\pi(1-\nu)}[(1-2\nu)I_{31}+3(\sigma_y^2+\sigma_x^2)I_{51}-3\sigma_y\sigma_x(I_{50}+I_{52})],\\
Q_{\sigma xx}(\mathbf{y}-\mathbf{x}) &= Q_{xx\sigma}(\mathbf{y}-\mathbf{x}),\\
Q_{\sigma x\sigma}(\mathbf{y}-\mathbf{x}) &= -\frac{\sigma_y \hat{x}}{8\pi(1-\nu)}[-(1-2\nu)I_{31}+3(\sigma_y^2 I_{50}+\sigma_x^2 I_{52}-2\sigma_y\sigma_x I_{51})],\\
Q_{\sigma\sigma x}(\mathbf{y}-\mathbf{x}) &= Q_{x\sigma\sigma}(\mathbf{y}-\mathbf{x}),\\
Q_{\sigma\sigma\sigma}(\mathbf{y}-\mathbf{x}) &= -\frac{\sigma_y}{8\pi(1-\nu)}\{(1-2\nu)[\sigma_x(I_{30}-2I_{32})+\sigma_y I_{31}]+3[\sigma_y^3 I_{51}-\sigma_y^2\sigma_x(I_{50}+2I_{52})+\sigma_y\sigma_x^2(2I_{51}+I_{53})-\sigma_x^3 I_{52}]\}.
\end{aligned}
\tag{35}
$$

References

[1] R.J. Asaro, W.A. Tiller, Interface morphology development during stress-corrosion cracking: Part I. via surface diffusion, Met. Trans. 3 (1972) 1789–1793.
[2] A.J. Bernoff, A.L. Bertozzi, T.P. Witelski, Axisymmetric surface diffusion: dynamics and stability of self-similar pinchoff, J. Stat. Phys. 93 (1998) 725–776.
[3] C.A. Brebbia, J.C.F. Telles, L.C. Wrobel, Boundary Element Techniques: Theory and Applications in Engineering, Springer-Verlag, Berlin, 1984.
[4] C.H. Chiu, H. Gao, Stress singularities along a cycloid rough-surface, Int. J. Solids Struct. 30 (1993) 2983–3012.
[5] J. Colin, J. Grilhè, N. Junqua, Surface instabilities of a stressed cylindrical whisker, Phil. Mag. A 76 (1997) 793–805.
[6] T.A. Cruse, D.W. Snow, R.B. Wilson, Numerical solutions in axisymmetric elasticity, Comput. Struct. 7 (1977) 445–451.
[7] I.S. Gradshteyn, I.M. Ryshik, Tables of Integrals, Series, and Products, Academic Press, San Diego, 2000.
[8] M.A. Grinfeld, Instability of the separation boundary between a nonhydrostatically stressed elastic body and a melt, Sov. Phys. Dokl. 31 (1986) 831.
[9] D.J. Haroldsen, D.I. Meiron, Numerical calculations of three-dimensional interfacial potential flows using the point vortex method, SIAM J. Sci. Comput. 20 (1998) 648–683.
[10] T.Y. Hou, J.S. Lowengrub, M.J. Shelley, Removing the stiffness from interfacial flows with surface tension, J. Comput. Phys. 114 (1994) 312.
[11] T.Y. Hou, J.S. Lowengrub, M.J. Shelley, Boundary integral methods for multicomponent fluids and multiphase materials, J. Comput. Phys. 169 (2001) 302–362.
[12] H.J. Jou, P.H. Leo, J.S. Lowengrub, Microstructural evolution in inhomogeneous elastic media, J. Comput. Phys. 131 (1997) 109–148.
[13] T. Kermanidis, A numerical solution for axially symmetrical elasticity problems, Int. J. Solids Struct. 11 (1975) 493–500.
[14] D.J. Kirill, S.H. Davis, M.J. Miksis, P.W. Voorhees, Morphological instability of a whisker, Proc. Roy. Soc. Lond. A 455 (1999) 3825–3844.
[15] V.D. Kupradze, T.G. Gegelia, M.O. Basheleishvili, T.V. Burchuladze, Three-dimensional Problems of the Mathematical Theory of Elasticity and Thermoelasticity, North-Holland Publishing Company, New York, 1979.
[16] C.G. Lambert, T.A. Darden, J.A. Board Jr., A multipole-based algorithm for efficient calculation of forces and potentials in macroscopic assemblies of particles, J. Comput. Phys. 126 (1996) 274–285.
[17] X. Li, Q. Nie, Surface diffusion on stressed solid surface, Commun. Comput. Phys. 2 (2007) 73–86.
[18] M. Mayr, The numerical solution of axisymmetric elasticity problems using an integral equation approach, Mech. Res. Commun. 3 (1976) 393–398.
[19] F.A. Nichols, W.W. Mullins, Surface- (interface-) and volume-diffusion contributions to morphological changes driven by capillarity, Trans. Metal. Soc. AIME 233 (1965) 1840–1848.
[20] Q. Nie, The nonlinear evolution of vortex sheets with surface tension in axi-symmetric flows, J. Comput. Phys. 174 (2001) 438–459.
[21] M. Nitsche, Axisymmtric vortex sheet motion: accurate evaluation of the principal value integral, SIAM J. Sci. Comput. 21 (3) (1999) 1066–1084.
[22] R. Panat, K.J. Hsia, D.G. Cahill, Evolution of surface waviness in thin films via volume and surface diffusion, J. Appl. Phys. 97 (2005) 13521.
[23] C. Pozrikidis, Boundary Integral and Singularity Methods for Linearized Viscous Flow, Cambridge University Press, 1992.
[24] C. Pozrikidis, Computation of periodic Green's functions of stokes flow, J. Eng. Math. 30 (1996) 79–96.
[25] Q. Nie, Y. Zhang, R. Zhao, Efficient semi-implicit schemes for stiff systems, J. Comput. Phys. 214 (2006) 521–537.
[26] Y. Saad, M.H. Schultz, GMRES: a generalized minimal residual algorithm for nonsymmetric linear systems, SIAM J. Sci. Stat. Comput. 7 (1986) 856–869.
[27] I. Schmidt, D. Gross, The equilibrium shape of an elastically inhomogeneous inclusion, J. Mech. Phys. Solids 45 (1997) 1521–1549.
[28] A. Sidi, M. Israeli, spectral convergence trapezoidal rule, J. Sci. Comput. 3 (1988) 201.
[29] M. Siegel, M.J. Miksis, P.W. Voorhees, Evolution of material voids for highly anisotropic surface energy, J. Mech. Phys. Solids 52 (2004) 1319–1353.
[30] B.J. Spencer, P.W. Voorhees, S.H. Davis, Morphological instability in epitaxially-strained dislocation-free solid films: linear stability theory, J. Appl. Phys. 73 (1993) 4955.
[31] B.J. Spencer, D.I. Meiron, Nonlinear evolution of the stress-driven morphological instability in a 2-dimensional semi-infinite solid, Acta Metall. Mater. 42 (1994) 3629–3641.
[32] H.A. Stone, L.G. Leal, Relaxation and breakup of an initially extended drop in an otherwise quiescent fluid, J. Fluid Mech. 198 (1989) 399–427.
[33] K. Thornton, N. Akaiwa, P.W. Voorhees, Large-scale simulations of Ostwald ripening in elastically stressed solids: I. Development of microstructure, Acta Mater. 52 (2004) 1353–1364.
[34] L. Ying, G. Biros, D. Zorin, A high-order 3d boundary integral equation solver for elliptic pdes in smooth domains, J. Comput. Phys. 219 (2006) 247–275.